Microscale Dynamics of Unsaturated Soil Behavior: Insights into Wetting and Drying Processes

Nabil Younes*,[1], Richard Wan[2], Antoine Wautier[3], Olivier Millet[4], and François Nicot[5]

[1] *LMGC, Univ Montpellier, CNRS, Montpellier, France*

[2] *Department of Civil Engineering, Schulich School of Engineering, University of Calgary, Calgary, Canada*

[3] *INRAE, Aix-Marseille University, UMR RECOVER, Aix-en-Provence, France*

[4] *LaSIE, UMR CNRS 7356, University of La Rochelle, La Rochelle, France*

[5] *University Savoie Mont-Blanc, ISTerre, Chambéry, France*

* *Corresponding author's email:* nabil.younes@umontpellier.fr

Abstract: In this study, we investigate the behavior of granular soils at the microscale, focusing on the dynamics of unsaturated conditions subjected to wetting and drying cycles. While the pendular regime is well-understood in the literature, the funicular and capillary regimes require more thorough analysis. Existing models are often unable to simulate realistic unsaturated soil conditions, i.e., in the funicular regime, motivating the development of a novel approach. We therefore propose a coupling between Lattice Boltzmann Method (LBM) and Discrete Element Method (DEM) to simulate capillary bridge dynamics and grain kinematics, respectively. This coupling has shown success in capturing crucial features such as the Soil-Water Characteristic Curve (SWCC) and the mean capillary stress. Through numerical simulations, we observe hysteresis phenomena in the mean capillary stress and suction during wetting and drying processes, highlighting the model's potential in representing unsaturated granular assemblies across all saturation regimes. Our findings highlight the importance of understanding microscale interactions in predicting the mechanical behavior of unsaturated soils, offering valuable insights for engineering applications, particularly for earthen dikes exposed to wetting and drying cycles induced by climate change.

Introduction

Earthen dikes are essential for flood protection in coastal areas, typically constructed from compacted granular soils under unsaturated conditions [1]. The presence of capillary bridges between the soil grains enhances the strength of the dikes, helping them to resist failure under hydraulic stress. However, these dikes are continuously exposed to environmental changes, such as rainfall and heatwaves, causing wetting and drying cycles that weaken their mechanical behavior and increase the risk of failure. These effects are largely driven by changes in the pore structure and fluid configuration within unsaturated soils at the mesoscopic scale, specifically within the Representative Elementary Volume (REV) [2]. Consequently, understanding the role

of hysteresis in unsaturated soils, which influences their mechanical properties during wetting and drying cycles, is vital to improving the prediction of dike stability.

The Soil-Water Characteristic Curve (SWCC), which represents the evolution of the suction[1] is a key tool for describing unsaturated soil behavior [3, 4]. However, most models of SWCC do not account for the hysteresis that occurs between the drying and wetting processes.

Numerous numerical models have been developed in the literature to investigate unsaturated granular soils. However, most of these models focus on the pendular regime, which represents only a small portion of the unsaturated soil spectrum (with a degree of saturation S_r of up to 20%) [5, 6]. When considering the funicular regime, many models rely on geometric criteria to simulate the rupture and merging of capillary bridges, which complicates the simulation of REVs [7]. This limitation highlights the need for more advanced modeling approaches to accurately capture the behavior of soils in higher saturation regimes.

The Lattice Boltzmann method (LBM) provides an effective solution to overcome the limitations of geometric criteria in simulating unsaturated soils [8, 9]. A phase-field-based LBM approach is well-suited for modeling all regimes: pendular, funicular, and capillary regimes. By solving both the Allen-Cahn and Navier-Stokes equations, this method enables the simulation of the dynamic behavior of capillary bridges. The flexibility of LBM lies in its ability to naturally represent complex processes, without requiring predefined geometric constraints or re-meshing, which is typically necessary in traditional methods.

To simulate REVs under unsaturated conditions, it is crucial not only to model the fluid dynamics and the formation of capillary bridges but also to account for the movement and dynamics of individual particles. Consequently, the coupling of the phase-field-based LBM model with the Discrete Element Method (DEM) becomes an excellent candidate [10]. It must be highlighted that in this work, YADE has been used for the DEM to handle the motion of the spherical particles [11]. The DEM-LBM coupling allows for the dynamic interaction between particles and the surrounding fluid, capturing both the fluid behavior and the motion of particles. This approach enables the simulation of the full range of capillary regimes, facilitating a more accurate representation of hysteresis behavior during wetting and drying cycles. Consequently, it provides deeper insights into the mechanics of unsaturated soils under varying water quantity at the micro-scale.

The paper is organized as follows: First, we present the phase-field-based LBM model as well as the evaporation-condensation approach used in our simulations. Then, we conduct simulations of unsaturated granular assemblies consisting of 3,750 spherical particles under a confining pressure of $\sigma^{\text{conf}} = 2$ kPa, analyzing their behavior in all capillary regimes during condensation and evaporation processes to highlight the hysteresis effect.

Numerical Models

In this study, we employ the Allen-Cahn phase-field-based LBM model, which has shown its capacity in handling liquid-gas interfaces. This model solves the modified Navier-Stokes equation to determine pressures and velocities, while solving the Allen-Cahn equation to track the

[1]The suction s is defined as the difference between the air pressure u_a and the water pressure u_w

capillary interface by calculating the phase parameter ϕ, which will be detailed thereafter.

Governing macroscopic equations

The Allen-Cahn equation is presented as follows

$$\frac{\partial \phi(\boldsymbol{r},t)}{\partial t} + \boldsymbol{\nabla}\cdot[\phi(\boldsymbol{r},t)\boldsymbol{u}] = \boldsymbol{\nabla}\cdot\{M[\boldsymbol{\nabla}\phi(\boldsymbol{r},t) - \lambda \boldsymbol{n}]\} \tag{1}$$

where $\boldsymbol{u}$ is the fluid velocity, M is the mobility, $\boldsymbol{n}$ is the outward unit-normal vector as shown in Figure 1a, $\phi(\boldsymbol{r},t)$ is the phase field parameter that is used to identify the regions occupied by the fluids (gas or liquid). The linear relation between fluid densities $\rho(\boldsymbol{r},t)$ and ϕ is given by

$$\rho(\boldsymbol{r},t) = \rho_g + \phi(\rho_\ell - \rho_g) \tag{2}$$

where ρ_g and ρ_ℓ are the gas and the liquid densities, respectively. Eq. 2 indicates that ϕ takes the value 0 for gas, 1 for liquid, and values within the range $]0;1[$ correspond to the fluid interface. It is important to note that at thermodynamic equilibrium of the capillary bridge, the distribution of $\phi(\xi)$ forms a smooth Heaviside function, as illustrated in Figure 1b. The phase field parameter at equilibrium, denoted ϕ_{eq}, has the following form:

$$\phi^{\text{eq}}(\xi) = \frac{1}{2} + \frac{1}{2}\tanh\left(\frac{2\xi}{W}\right) \tag{3}$$

where ξ is the orthogonal local variable crossing through the interface as shown in Figure 1a. Finally, in Eq. 1 the parameter λ is defined as $\lambda = \mathrm{d}\phi^{\text{eq}}/\mathrm{d}\xi$.

The modified multi-phase Navier-Stokes equations for incompressible fluids read

$$\begin{gathered}\rho\left(\frac{\partial \boldsymbol{u}}{\partial t} + \boldsymbol{u}\cdot\boldsymbol{\nabla}\boldsymbol{u}\right) = -\boldsymbol{\nabla}p + \boldsymbol{\nabla}\cdot\boldsymbol{\tau} + \boldsymbol{F}_s + \boldsymbol{G} \\ \boldsymbol{\nabla}\cdot\boldsymbol{u} = 0\end{gathered} \tag{4}$$

where p is the pressure, $\boldsymbol{\tau} = \rho\nu\left(\boldsymbol{\nabla}\boldsymbol{u} + \boldsymbol{\nabla}\boldsymbol{u}^T\right)$ is the viscous stress tensor (ν is the kinematic viscosity), $\boldsymbol{G}$ is the body force, and $\boldsymbol{F}_s$ is the surface tension term defined as follows

$$\boldsymbol{F}_s = \mu_\phi \boldsymbol{\nabla}\phi \tag{5}$$

where μ_ϕ is the chemical potential $\mu_\phi = 4\beta\phi(\phi-1)\left(\phi - \frac{1}{2}\right) - k\boldsymbol{\nabla}^2\phi$ with

$$k = \frac{3}{2}\gamma W; \beta = \frac{12\gamma}{W} \tag{6}$$

and γ is the surface tension and W is the interface width. The detailed LBM schemes, including the boundary conditions (bounce-back and wetting conditions), are provided in [8, 10].

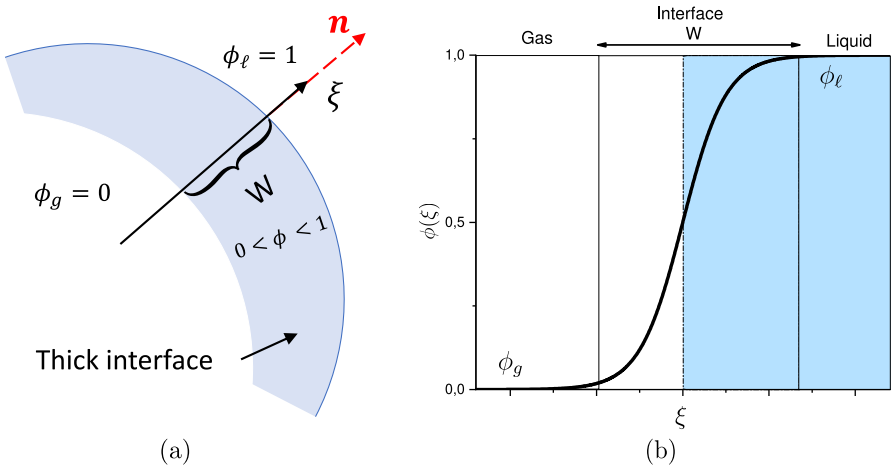

(a) (b)

Figure 1: (a) Scheme of the smooth interface. $\phi \in \{0; 1\}$ corresponds to the bulk fluid, gas, and liquid, respectively. And $\phi \in]0; 1[$ corresponds to the thick interface of width W. (b) The smooth evolution of ϕ through the interface whose thickness is W (smooth Heaviside function). ϕ_ℓ and ϕ_g correspond to liquid and gas phase parameters, respectively.

Capillary forces

For all regimes, capillary forces coming from capillary bridges are calculated as follows [8]

$$\hat{\boldsymbol{F}}_f = \underbrace{\int_\Omega \boldsymbol{\sigma}_f \boldsymbol{n}_\Omega \, \mathrm{d}S}_{\boldsymbol{F}_\mathrm{p}} + \underbrace{\gamma \int_\Gamma \boldsymbol{m} \, \mathrm{d}\ell}_{\boldsymbol{F}_\gamma} \tag{7}$$

where Ω represents the integrated domain, $\boldsymbol{\sigma}_f = -p\mathrm{I} + \boldsymbol{\tau}$ denotes the fluid stress tensor with I as the identity tensor in $\mathbb{R}^3$, $\boldsymbol{n}_\Omega$ is the outward unit-normal vector to the domain Ω. dS and $d\ell$ represent infinitesimal patch of area and infinitesimal small segment, respectively. The term Γ denotes the intersection of Ω with the capillary interface, γ is the surface tension, and $\boldsymbol{m}$ is the tangent vector of the gas-liquid interface. For more details on the formulation and discretization of capillary force calculations, readers can refer to [8].

Evaporation and condensation processes

At thermodynamic equilibrium, the phase field parameter ϕ must satisfy the equilibrium condition, expressed as $\phi(\xi) = \phi^{\mathrm{eq}}(\xi)$. Differentiating $\phi^{\mathrm{eq}}(\xi)$ from Eq. 3 results in the following expression:

$$\mathrm{d}\phi = \frac{4}{W}\phi(1-\phi)\mathrm{d}\xi \tag{8}$$

Here, $\mathrm{d}\phi$ represents the infinitesimal change in ϕ at equilibrium, while $\mathrm{d}\xi$ denotes the infinitesimal displacement along the interface within the capillary bridge. This equation establishes the link between the variations in the phase field parameter and the corresponding positional changes of the interface.

The proposed numerical approach allows for the imposition of evaporation and condensation processes as follows:

$$\phi^{\mathrm{e}}(\xi) = \phi^{\mathrm{eq}}(\xi) - \Delta\phi(\Delta\xi) \tag{9a}$$

$$\phi^{\mathrm{c}}(\xi) = \phi^{\mathrm{eq}}(\xi) + \Delta\phi(\Delta\xi) \tag{9b}$$

Here, $\phi^{\mathrm{e}}(\xi)$ and $\phi^{\mathrm{c}}(\xi)$ represent the phase field parameter profiles following the evaporation and condensation processes, respectively.

Figure 2 illustrates the equilibrium profile $\phi^{\mathrm{eq}}(\xi)$ (black curve), along with the modified profiles after condensation (red curve) and evaporation (blue curve), corresponding to an interface displacement of $\Delta\xi = \pm 1$ lattice unit. As shown in Figure 2, significant variations in ϕ occur only at the liquid-gas interface, while in the bulk regions the phase field parameter remains nearly constant $\phi \in \{0; 1\}$.

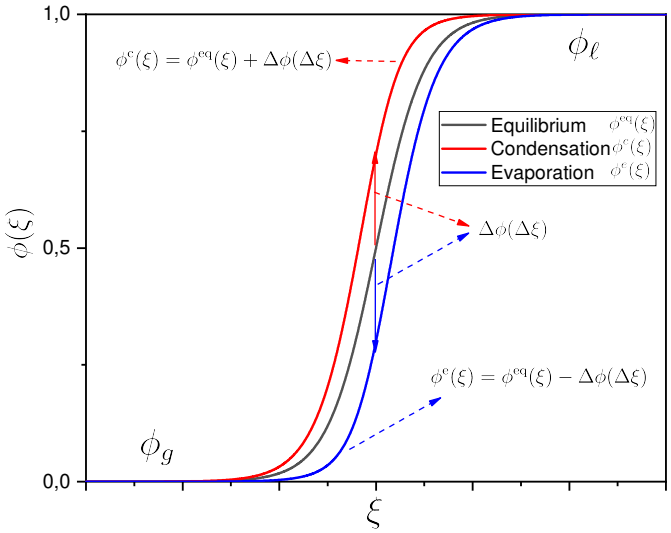

Figure 2: Profiles of condensed and evaporated liquid-gas capillary interfaces $\phi^{\mathrm{c}}(\xi)$ and $\phi^{\mathrm{e}}(\xi)$, respectively for $\Delta\xi = 1$.

A sensitivity analysis of the parameter $\Delta\xi \in]0; 2]$ was performed using three spherical particles arranged in a equilateral triangle to calculate capillary forces. For values $0 < \Delta\xi \leq 1$, the results remained unchanged. For $\Delta\xi > 1$, the phase-field variable ϕ exceeds 1, which is physically unacceptable. Therefore, the value $\Delta\xi = 1$ is adopted for the remained of this study. The corresponding demonstration is omitted here as it falls outside of the scope of this study.

Hysteresis of unsaturated granular assemblies

In this section, we apply the DEM-LBM coupling model to simulate the mechanical behavior of a granular assembly composed of 3,750 spherical grains following a uniform grain size distribution such that $D_{\max}/D_{\min} = 1.35$ with $D_{\max} = 108\,\mu\mathrm{m}$, and $D_{\min} = 80\,\mu\mathrm{m}$. The computational domain size consists of $N_X = N_Y = N_Z = 350$ lattice nodes in the $x-$, $y-$, $z-$directions,

respectively. The spatial discretization is uniform, with $\Delta x = \Delta y = \Delta z = 5 \times 10^{-6}$ m. The preparation of the sample involves isotropic confinement under a confining pressure of $\sigma^{\text{conf}} = 2$ kPa. The DEM parameters are summarized in Table 1. We initiate the simulation

Parameters	Values	Units
Density ρ_s	2,600	kg.m^{-3}
Stiffness E	110	MPa
Stiffness ratio (α)	0.3	–
Inter-particle friction angle	30	°
$\{D_{\min}; D_{\max}\}$	{80; 108}	µm
Number of particles	3,750	–

Table 1: YADE mechanical parameters for the grains. Same parameters are used in [10].

at a high saturation level ($S_r \approx 96\%$) to ensure a nearly continuous water phase, minimizing the variability in capillary bridge configurations. Evaporation is then applied until $S_r \approx 6\%$, followed by condensation to approach full saturation[2].

The matric suction used here can be estimated as the average of all local suctions s^i at capillary menisci weighted by their respective volumes as in [10]

$$s = \frac{1}{V_w} \sum_{i=1}^{\text{N}^{\text{clusters}}} \overbrace{(u_a - u_w^i)}^{s^i} V_w^i \tag{10}$$

where V_w is the total water volume, $\text{N}^{\text{clusters}}$ is the number of water clusters within the sample[3], u_w^i is the pore water pressure within the i^{th} water cluster, and V_w^i is the volume of the i^{th} water cluster.

Figure 3 illustrates the evolution of suction s as a function of the degree of saturation for the same wetting angle $\theta = 25°$ for both cycles. The figure clearly demonstrates the hysteresis effect resulting from the evaporation and condensation cycles. In addition, the suction s during evaporation is higher than during condensation, consistent with the typical behavior observed in SWCC.

[2]The suction is influenced by the initial capillary bridge configuration within the granular assembly, but this analysis is beyond the scope of this work.

[3]The number of liquid clusters is defined as the total number of connected liquid volumes, where a connected volume refers to a continuous liquid bridging one or more particles.

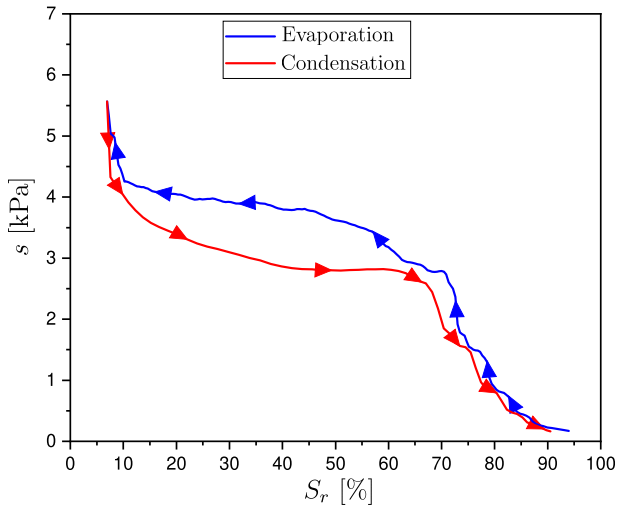

Figure 3: The evolution of suction s [kPa] in terms of degrees of saturation S_r during evaporation and condensation processes for the same wetting angle $\theta = 25°$. For a clear visualization, arrows indicating the path directions—evaporation or condensation—are added.

The capillary stress $\boldsymbol{\sigma}^{\text{cap}}$ can be calculated indirectly using both Love-Weber (contact stress between particles) $\boldsymbol{\sigma}^{\text{cont}}$ and total stress $\boldsymbol{\sigma}$ formulae as follows:

$$\boldsymbol{\sigma}^{\text{cap}} = \boldsymbol{\sigma} - \boldsymbol{\sigma}^{\text{cont}}. \tag{11}$$

Since the confining pressure is remained constant at $\sigma^{\text{conf}} = 2$ kPa in all directions during the simulation, the sample is isotropic. Therefore, we calculate the mean capillary stress p^{cap} as the average of three principal components of $\boldsymbol{\sigma}^{\text{cap}}$:

$$p^{\text{cap}} = \frac{1}{3}\text{Tr}\left(\boldsymbol{\sigma}^{\text{cap}}\right). \tag{12}$$

The evolution of the mean capillary stress p^{cap} is depicted in Figure 4. While the sample undergoes evaporation, the mean capillary stress increases until reaching a threshold at $S_r \approx 68\%$, below which it begins to decrease. Similarly, during the condensation process, starting from $S_r \approx 6\%$, the mean capillary stress rises until it peaks at $S_r \approx 50\%$ and then decreases toward zero as the system approaches full saturation. The peak values of the mean capillary stress, p^{cap}, differ between the two processes: $p^{\text{cap}} = 3.05$ kPa during evaporation and $p^{\text{cap}} = 2.37$ kPa during condensation. This variation results from the suction differences observed between the evaporation and condensation processes, as illustrated earlier in Figure 3. In addition, an intriguing observation arises from the rate at which the mean capillary stress increases or decreases. While the maximum value of p^{cap} is reached earlier during condensation, its subsequent decrease is more gradual compared to the sharper decline seen during evaporation. This behavior could be related to the topological differences in capillary bridges and air bubbles within the sample, a phenomenon that will be explored further in this study.

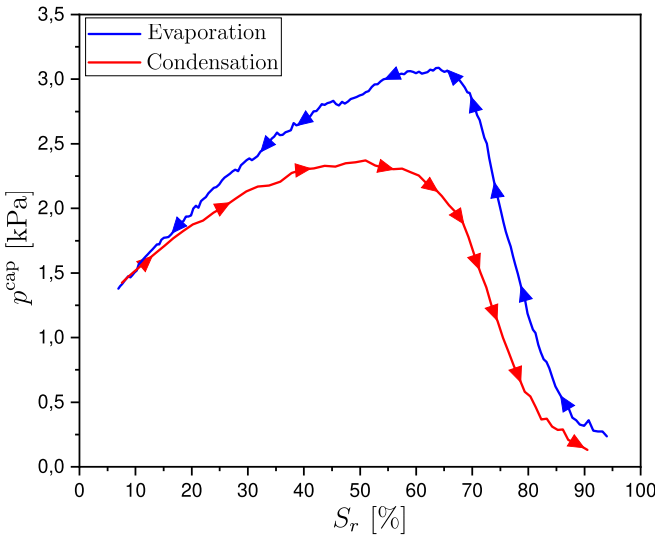

Figure 4: The evolution of mean capillary stress p^{cap} [kPa] in terms of degrees of saturation S_r during evaporation and condensation processes for a wetting angle of $\theta = 25°$. For a clear visualization, arrows indicating the path directions—evaporation or condensation—are added.

To understand the physics behind this result, the number of water clusters and air bubbles are investigated, as shown in Figure 5. Panel (a) reveals that the evaporation process begins in the *capillary* regime, characterized by a single large water cluster. As evaporation proceeds, only one capillary bridge exists until the degree of saturation reaches $S_r \approx 68\%$. Beyond this point, the number of water clusters begins to increase. This corresponds to the stage where the mean capillary stress reaches its peak value and then starts to decrease. During evaporation, the number of air bubbles peaks at $S_r \approx 68\%$, which coincides with the time when p^{cap} reaches its maximum. The formation of a significant number of air bubbles increases the curvature of the liquid-gas interface, leading to stronger capillary forces. This contributes to the rise in mean capillary stress. Interestingly, the number of air bubbles closely follows the evolution of the mean capillary stress throughout the process.

In the condensation process, the number of water clusters increases slightly at low degrees of saturation before gradually decreasing toward 1 as the system approaches full saturation. The mean capillary stress, p^{cap}, reaches its peak at $S_r \approx 51\%$. However, at this degree of saturation, there are 138 capillary bridges present, unlike the evaporation process where a single capillary bridge dominates at the peak. Despite the larger number water clusters, approximately 98% of the water volume is still contained within a single large capillary bridge. This observation suggests that the system can be effectively approximated as having one dominant cluster of capillary bridges, with the remaining bridges playing a secondary role in moderating the decrease in mean capillary stress as the saturation increases.

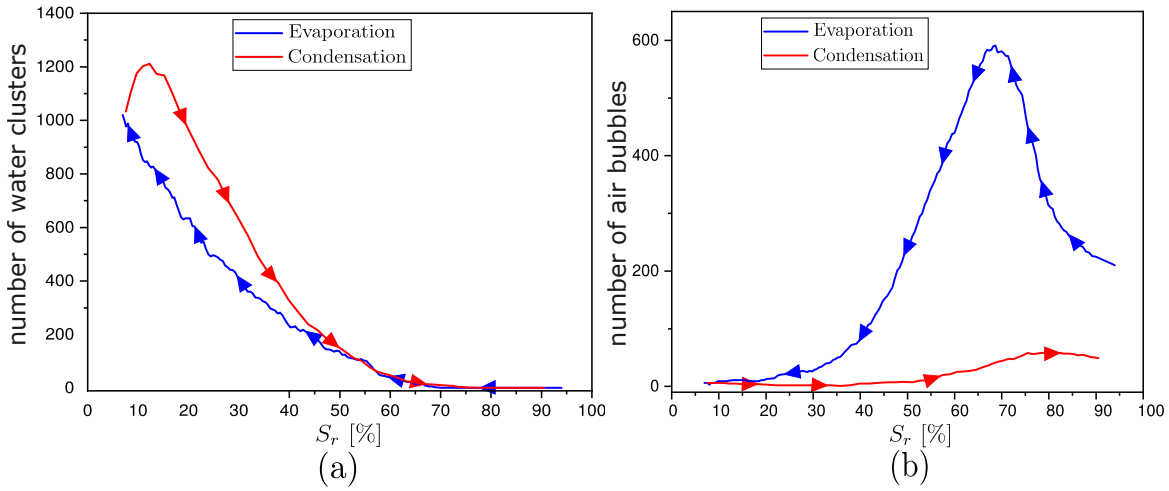

Figure 5: The evolution of the number of (a) water clusters and (b) air bubbles in terms of degrees of saturation S_r during evaporation and condensation processes for a wetting angle of $\theta = 25°$. For a clear visualization, arrows indicating the path directions—evaporation or condensation—are added.

Regarding the number of air bubbles, they increase slightly during the wetting process, but remain much fewer compared to those observed during evaporation. As the saturation reaches $S_r \approx 80\%$, air bubbles start to vanish entirely, and the mean capillary stress decreases at a similar rate to that observed during evaporation. The larger number of air bubbles in the evaporation process may explain why the mean capillary pressure is higher during evaporation than during condensation.

The execution time of the simulations is approximately 24 hours for a complete evaporation and condensation process using Tesla-series GPU cards.

Conclusion

This paper uses a DEM-LBM coupling and an evaporation-condensation method to study the behavior of unsaturated granular materials during wetting and drying cycles across all regimes (pendular, funicular, and capillary). The phase-field Lattice Boltzmann Method (LBM) simulates liquid bridges and capillary effects, while the Discrete Element Method (DEM) models the dynamics of spherical grains using YADE. A new method for simulating evaporation and condensation is also introduced. Several important findings emerge from our study. Despite maintaining a constant wetting angle between evaporation and condensation, both suction and mean capillary stress exhibit hysteresis during the simulation. This behavior indicates that hysteresis is influenced not only by the wetting angle but also by the topology of capillary bridges and air bubbles within the sample. Notably, we demonstrate that the numbers of capillary bridges and air bubbles differ between evaporation and condensation processes.

In conclusion, the DEM-LBM coupling proves effective in capturing all possible regimes in unsaturated soils. Moreover, this coupling, along with the proposed condensation and evaporation method, provides valuable insights into the effect of hysteresis on the mean capillary

stress, commonly referred to as apparent cohesion in unsaturated soils. In future work, this coupling will be applied to practical macro-scale applications, such as the stability assessment of dikes, incorporating additional energetic criteria like the second-order work criterion.

References

[1] W J Likos and Ning L. Unsaturated soil mechanics. *ed: John Wiley and Sons Inc., New Jersey*, 2004.

[2] R Wan, F Nicot, and F Darve. *Failure in geomaterials: a contemporary treatise*. Elsevier, 2017.

[3] R Wan, M Pouragha, M Eghbalian, J Duriez, and T Wong. A probabilistic approach for computing water retention of particulate systems from statistics of grain size and tessellated pore network. *International Journal for Numerical and Analytical Methods in Geomechanics*, 43(5):956–973, 2019.

[4] M Th Van Genuchten. A closed-form equation for predicting the hydraulic conductivity of unsaturated soils. *Soil science society of America journal*, 44(5):892–898, 1980.

[5] F Soulie, M. S. El Youssoufi, F Cherblanc, and C Saix. Capillary cohesion and mechanical strength of polydisperse granular materials. *The European Physical Journal E*, 21(4):349–357, 2006.

[6] J Duriez, M Eghbalian, R Wan, and F Darve. The micromechanical nature of stresses in triphasic granular media with interfaces. *Journal of the Mechanics and Physics of Solids*, 99:495–511, 2017.

[7] M Miot, G Veylon, A Wautier, P Philippe, F Nicot, and journal=Granular Matter volume=23 number=3 pages=1–18 year=2021 publisher=Springer Jamin, F. Numerical analysis of capillary bridges and coalescence in a triplet of spheres.

[8] N Younes, Z Benseghier, O Millet, A Wautier, F Nicot, and R Wan. Phase-field lattice boltzmann model for liquid bridges and coalescence in wet granular media. *Powder Technology*, page 117942, 2022.

[9] Z Benseghier, O Millet, P Philippe, A Wautier, N Younes, and E Liberge. Relevance of capillary interfaces simulation with the shan–chen multiphase lb model. *Granular Matter*, 24(3):1–18, 2022.

[10] N Younes, A Wautier, R Wan, O Millet, F Nicot, and R Bouchard. Dem-lbm coupling for partially saturated granular assemblies. *Computers and Geotechnics*, 162:105677, 2023.

[11] V Šmilauer, E Catalano, B Chareyre, S Dorofeenko, J Duriez, A Gladky, J Kozicki, C Modenese, L Scholtès, L Sibille, et al. Yade reference documentation. *Yade Documentation 3rd ed.*, (1), 2021.